Global Alfvén Eigenmodes in the H-1 heliac

M.J. Hole[1], B. D. Blackwell[1], G. Bowden[1], M. Cole[2], A. Könies[2], C. Michael[1], F. Zhao[1] and S. R. Haskey[3]

[1] Research School of Physics and Engineering, Australian National University, Acton 0200, ACT Australia

[2] Max Planck Institute for Plasma Physics, D-17491 Greifswald, Germany

[3] Princeton Plasma Physics Laboratory, P.O. Box 451, Princeton, New Jersey 08543-0451, USA

Abstract. Recent upgrades in H-1 power supplies have enabled the operation of the H-1 experiment at higher heating powers than previously attainable. A heating power scan in mixed hydrogen/helium plasmas reveals a change in mode activity with increasing heating power. At low power (< 50 kW) modes with beta-induced Alfvén eigenmode (BAE) frequency scaling are observed. At higher power modes consistent with an analysis of nonconventional global Alfvén Eigenmodes (GAEs) are observed, the subject of this work. We have computed the mode continuum, and identified GAE structures using the ideal MHD solver CKA and the gyrokinetic code EUTERPE. An analytic model for ICRH-heated minority ions is used to estimate the fast ion temperature from the hydrogen species. Linear growth rate scans using a local flux surface stability calculation, LGRO, are performed. These studies demonstrate drive from the radial spatial gradient of circulating particles whose speed is significantly less than the Alfvén speed, and are resonant with the mode through harmonics of the Fourier decomposition of the strongly-shaped heliac magnetic field. They reveal drive is possible with a small ($n_f/n_0 < 0.2$) hot energetic tail of the hydrogen species, for which $T_f > 300$ eV. Local linear growth rate scans are also complemented with global calculations from CKA and EUTERPE. These qualitatively confirm the findings from the LGRO study, and show that the inclusion of finite Larmor radius effects can reduce the growth rate by a factor of up to 10, and increases the marginal stability fast ion temperature by a factor of two. Finally, a study of damping of the global mode with the thermal plasma is conducted, computing continuum damping , and the damping arising from finite Larmor radius and parallel electric fields (via resistivity). We find that continuum damping is of order 0.1% for the configuration studied. A similar calculation in the cylindrical plasma model produces a frequency 35% higher and a damping 30% of the three dimensional result: this confirms the importance of strong magnetic shaping to the frequency and damping. The inclusion of resistivity lifts the damping to $\gamma/\omega = -0.189$. Such large damping is consistent with experimental observations that in absence of drive the mode decays rapidly (~ 0.1 ms).

PACS numbers:

1. Introduction

Alfvénic instabilities in fusion plasmas are of programmatic concern due to their known potential to cause particle ejection, thereby preventing heating by thermalisation ([1] and the review [2] and references therein). Expelled energetic particles can also damage the first wall, and a fusion reactor can only tolerate fast particle losses of a few per cent [3]. Another motivation for the study of Alfvén eigenmodes is their potential use as a diagnostic for the plasma, particularly through the tool of magnetohydrodynamic (MHD) spectroscopy. In recent years this has been expanded beyond safety factor or q profile inference to include temperature profile [4, 5].

There have been numerous previous experiments and theoretical studies of Alfvén eigenmodes in stellarator devices. In W7-AS, global Alfvén eigenmodes (GAEs), destabilized by circulating particles were first observed [6]. Other gaps have also been round in stellarators, including the helicity-induced-Alfvén eigenmode (HAE), first observed on LHD [7]. Extensive characterization of beam-driven energetic ion driven Alfvén eigenmodes has also been carried out in LHD where core-localized toroidal Alfvén eigenmodes (TAEs) of $n < 5$ were detected as well as edge-localized GAEs, and extensive comparison of measurements with CAS3D modelling was carried out [8]. Furthermore, TAE bursting was found associated with significant fast particle losses [9]. More recently in TJ-II GAEs were found [10], and extensive comparison of measured mode structures with experiments were made by way of frequency-gap diagrams, and eigenmode analysis including the coupling with sound-waves. Whilst many studies have focused on the observation and properties of various classes of Alfvén eigenmodes, there has not been as much attention directed towards computing their stability, mainly because they are driven in experiments with extensive beam-driven fast particle population. On H-1, however, beams are not present and the only mechanism for generation of fast particles is through the ion-cyclotron resonance heating. Thus, the observation of Alfvénic modes motivates studying their destabilization by relatively low energy ions. The observation of low frequency modes has motivated the study of the coupling to the sound continuum, which is a feature of beta-induced Alfvén eigenmodes (BAEs), commonly observed in tokamaks [11].

Spontaneously excited MHD fluctuations in 0.5 T hydrogen/helium ion cyclotron resonance heated (ICRH) H-1 heliac plasmas [12] have been reported since 2004 [13]. These results motivated experimental studies on the configuration dependence of mode activity [14, 15, 16], as well as the installation of several new diagnostic systems and techniques to improve the understanding of the nature of these modes. These include a helical magnetic probe array [17], a synchronous imaging technique [18] as well as associated analysis techniques such as periodic data-mining [19] and tomographic inversion [20].

Study of the detailed mode physics for a particular configuration in the H-1 heliac was pioneered by Pretty and Blackwell *et al* [14, 15] and the effects of finite compressibility by Bertram *et al* , [21, 5] and more recently by Haskey *et al* [22]. Bertram

et al [21] extended a reduced-dimension cylindrical stellarator ideal-MHD normal-mode model to include a vacuum region, and describe magnetic fluctuations in the H-1 heliac. In H-1, the magnetic geometry is defined by κ_H, a parameter measuring relative coil currents which is held constant during a discharge. Different values of κ_H correspond to different plasma parameters, flux-surface geometries and rotational transform $\iota = 1/q$ profiles (see [15] for more details). Analysis focused on the two lowest frequency GAEs at $\kappa_H = 0.54$, the $(m, n) = (4, 5)$ and $(7, 9)$ modes, and showed that for the low temperature $T_i = T_e = 20$ eV and low density $n_e(0) = 2.5 \times 10^{18}$ m^{-3} plasma conditions the $(7, 9)$ and $(4, 5)$ modes have a frequency of 20.3 kHz and 114.1 kHz, respectively, with the measured frequency of approximately 40 kHz. These plasmas had a mixed helium/hydrogen composition with gas flow ratio of one part hydrogen to two parts helium (H:2He).

Mirnov coil data suggested the $(4, 5)$ mode a better phase fit to the data, with the $(7, 9)$ a closer amplitude profile fit. Building on this work, Bertram *et al* [5] developed a part-analytical, part-numerical ideal MHD analysis of low frequency compressible modes. Using ideal MHD codes CAS3D [23] and CONTI [24] the compressible ideal MHD spectrum for H-1 plasmas with $\kappa_H = 0.30$ was computed, and low frequency modes lying within the acoustic-Alfvén gap studied. Several discrete (4,5) modes were computed within the gap for κ_H=0.30, with frequency below 35 kHz. By assuming a hollow temperature profile, Bertram *et al* were able to show the gap frequency scaling of κ_H agrees with the observed frequency dependence with configuration. Indeed, probe measurements shown here show slightly inverted temperature profiles at higher powers (> 50 *kW*) characteristic of edge electron heating, and helium line ratio measurements showed considerably hollow T_e measurements [25]. At lower heating power of 30 kW, Haskey *et al* [22] compared the experimentally observed behaviour of four "clusters" of MHD mode activity with different κ_H. Each cluster [16] represents a grouping of fluctuations with similar magnetic probe phase signature to the diagnostic array. Comparisons of the different clusters with compressible ideal-MHD predictions using CAS3D and CONTI revealed the presence of beta-induced gaps, Alfvén-acoustic gaps and low frequency discrete eigenmodes that were representative of observed modes in each cluster. Mode characterisation by examination of signal properties from a broader range of diagnostics has also been conduced in TJ-II. [26]

In H-1, a synchronous imaging technique [18] was used to acquire high resolution images of a typical mode for each cluster: these were tomographically inverted in magnetic coordinates to provide the radial structure of a set of Fourier basis modes. [22] MHD mode structures are a function of the density profile. By assuming a density profile linear in toroidal flux s candidate BAE and nonconventional global Alfvén eigenmodes (NGAE) were computed. [27] Comparisons to experimental data revealed that the BAE mode was a slightly better fit to the observed radial structure, although it was noted that the emissivity is a strong function of density profile. In H-1 only these selected modes have been analyzed and published, with a wider variety of coherence modes generally observed.

In this work, we focus on drive and damping of low frequency wave activity for a particular magnetic configuration, as a function of radio frequency (RF) power. Our analysis of ICRH drive follows the analysis of Mishchenko *et al* [28], who compute drive from an anisotropic distribution function due to ICRH-heated minority ions modelled in W7-X stellarator geometry. For these model calculations, perpendicular temperature was determined by the ICRH power deposition profile, modelled by Dendy *et al* [29] and Stix [30]. Local Flux surface mode drive is computed as a function of fast ion temperature using the code LGRO [31], and global calculations have also been performed using codes CKA [32] and EUTERPE [33]. Additionally, estimates of continuum damping have been made using a complex contour integration method [34]. This study represents the first study of *both* mode drive and damping in the H-1 heliac. The manuscript is structured as follows: Sec. II introduces the experimental data, while Sec. III focuses on modelling the drive and damping of modes using both local flux surface and global stability calculations, starting with the introduction of the assumed form of the fast ion distribution function, a linear analysis then global stability calculations, together with continuum and resistive damping. Finally, Sec. IV contains concluding remarks.

2. Experiments

A power scan was performed over a set of 10 discharges, #86508 - #86517, where the total RF power P_{tot} was stepped down from 80kW to 14kW. The objective of the scans was to examine the variation in mode behaviour (frequency and amplitude) as a function of RF power level. The discharges were heated using minority ICRH having B=0.5T, with a magnetic configuration characterised by helical coil current fraction $\kappa_H = 0.33$ and ι profile shown in Fig. 1. The ion cyclotron resonance line in the cylindrical $[R, z]$ cross-section is a straight line passing through the magnetic axis, and entering the plasma at an angle 30 deg from the cross-section symmetry axis. A 21-channel imaging interferometer produced time and position resolved line integrated density data. Figure 2 shows the evolution of the central line averaged electron density for all discharges. All discharges achieve an approximate equilibrium flat-top between $t = 20$ms and $t = 55$ms (at which point the RF power is stepped down gradually over 5ms). While spatial profiles of n_e did not change in time beyond density flat-top, the profiles did change with RF heating power. Figure 3 shows the (symmetrized) line-averaged density (for a path length corresponding to the central chord) as a function of $s = (z/a)^2$, where z is the height of the horizontal chord in the outboard mid-plane, and fitted to a polynomial in s, with $a = 0.19$ m being the minor radius in the vertical direction. The polynomial fits, which without Abel inversion, only approximately represent the spatial profile of local density profile $n_e(s)$, have inspired the $1 - s$ profile used in the analysis of Sec. 3, with the central density matching the density of the core fit in Fig. 3. Here, the polynomial fitted is second order in s, with $n_{e,fit}(s) = (p_1 s + p_0)(1 - s) + (n_0 - p_0)$, with p_1, p_0 and n_0 constants fitted using a simplex method. Finally, electron temperature

measurements, shown in Fig. 4 are available from ball pen probes [35]. While they show a complicated dependence with radial position, there is some evidence for a hollow electron temperature profile at higher power. For calculations in Sec. 3, we have taken T_e to be constant (10eV) as a function of space and power.

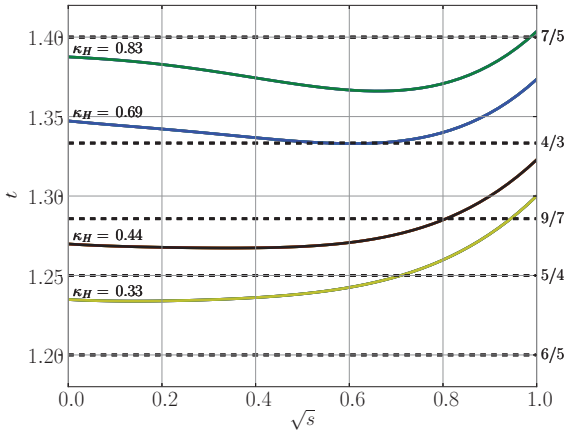

Figure 1. Rotational transform profile for H-1 for a range of κ_H values, as a function of square root of toroidal flux $\sqrt{s}$. This work focuses on $\kappa_H = 0.33$.

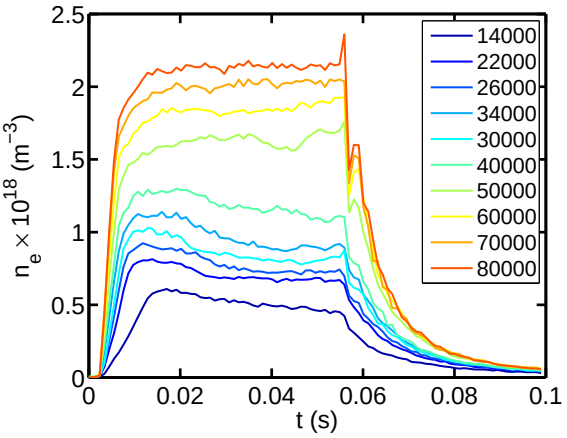

Figure 2. Time evolution of central chord of electron density profile for discharges #86508 at $P_{tot} = 80$ kW to #86517 at $P_{tot} = 14$ kW. The legend denotes the RF power in Watts. Discharges # 86514 and # 86508 correspond to 34000 W and 80000 W traces, respectively.

Magnetic oscillations were observed in all discharges. Figure 5 shows magnetic spectra for illustrative discharges #86514 (34 kW) and #86508 (80 kW). For the low frequency branch at approximately 10 kHz, a mode analysis computes the poloidal (m) and toroidal (n) mode numbers $(m, n) = (4, -5)$. This is the mode that has systematically been studied in a range of experiments [13, 14, 16, 21, 5, 22]. The 40 kHz mode that appears at 20 ms has a mode number that is indeterminate, and there is

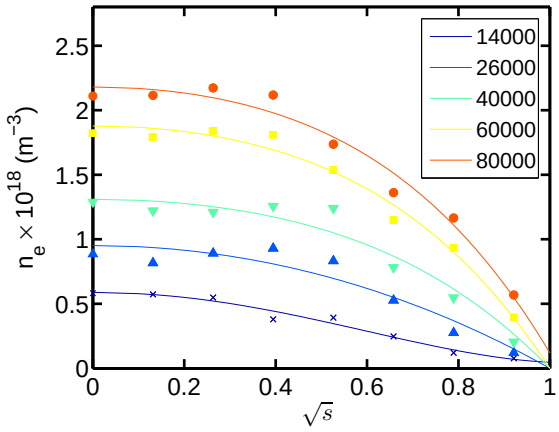

Figure 3. Line-averaged density profiles (for a given constant 17cm path length corresponding to the central horizontal plasma diameter in the outboard mid-plane) at $t = 0.20$s as a function of $\sqrt{s}$, together with polynomial fits in s. The legend gives the polynomial fits to the density profile for various RF power levels in Watts. Circle, square, down-triangle, up-triangle, and cross are for 80 kW, 60 kW, 40 kW, 26 kW, and 14 kW respectively.

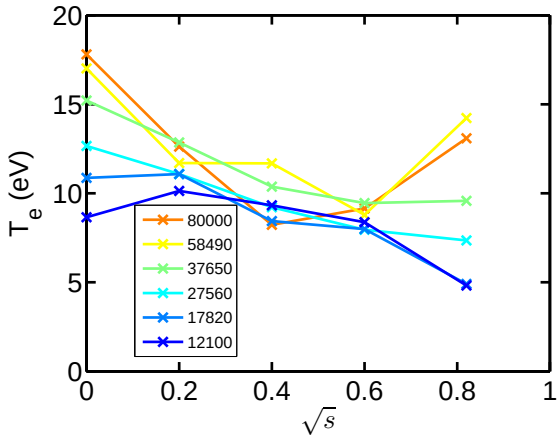

Figure 4. Ball pen probe measurements (cross-hairs) of electron temperature for $\kappa_H = 0.33$, as a function of $\sqrt{s}$. The curves correspond to different power levels P_{tot} in Watts.

evidence for a mixture of multiple modes, including $(m, n) = (4, -5)$. However the scaling of the frequency of this mode with configuration is not understood.

Overlaid on both figures is the predicted evolution of the GAE frequency computed in Sec. 3, as well as the lowest BAE geodesic solution computed for $\kappa_H = 0.30$ in Bertram *et al* [5], at 9.4 kHz. In both cases the mode numbers are assumed to be $(m, n) = (4, -5)$ and the mode frequency is computed at 20 ms. For the higher frequency GAE mode, the time evolution of the mode is computed from the $1/\sqrt{(n_e(0))}$ scaling, where $n_e(0)$ is the core electron density chord. This is reasonable as the mode peak is at $s \approx 0.2$. The lower frequency mode is an Alfvén acoustic type solution whose

frequencies scale with the adiabatic sound speed $c_s \approx \sqrt{\beta} v_A$, where $v_A = B/\sqrt{\mu_0 \rho}$ is the Alfvén speed. As the temperature is low, the impact of variations on the temperature on frequency evolution can hence be significant. The BAE mode of Bertram *et al* is an edge mode, with a peak at $s = 0.6$. We have hence computed the time evolution of the mode from $c_s \propto \sqrt{Te(s = 0.6)}$. We have also added the time evolution of the kinetic accumulation frequency $\omega_{CAP} = 1/R_0\sqrt{2T_i/m_i(7/4 + T_e/T_i)}$ determined from large aspect ratio tokamak theory [36]. The difference between the predicted BAE frequencies can not be resolved within uncertainty of the experimental measurements: both agree reasonably well with the low frequency oscillations evident in Fig. 5(a). In the remainder of this work we focus on physics modelling of this higher frequency mode, and make the assumption $(m, n) = (4, -5)$. For this mode, an additional experiment was carried out to determine the mode's damping rate, where the RF power was dropped from 80 to 50kW and the decay of the 40kHz mode is measured. It was found that the mode decays on timescales on the order of ≈ 0.1ms, which is at the limit of the time constant of the RF systems. In the core of the plasma, the time-constants for changes in T_e and n_e are greater than 0.1ms, suggesting that the mode drive is indeed related directly to RF fast particle effects rather than the thermal plasma profiles, and also gives an upper bound for the mode damping rate, to be compared with simulations in Sec. 3.3.

3. GAE Modelling

For the magnetic field configuration of $\kappa_H = 0.33$ we have computed the shear Alfvén continuum using CONTI. Figure 6 shows the continuum. Global Alfvén eigenmodes can reside at the stationary point in the Alfvén frequency, located at radial localisation of $s = 0.116$ and frequency of 45.7 kHz. At this location the Alfvén frequency is a maximum, and so it corresponds to a non-conventional GAE (NGAE) [37]. Conditions for a NGAE are most easily satisfied in low-shear current-less stellarators, such as H-1. For simplicity, we refer to this NGAE as a GAE in the remainder of the work.

We have applied the analysis of RF drive calculations in Mishchenko *et al* for W-7X geometry of a TAE mode to H-1. [28] Measurements of the distribution function and hence fast ion temperature from ICRH heating in H-1 are unavailable. Instead, we have used an isotropic Maxwellian distribution function for the minority ions on the cyclotron resonance layer

$$f_0(s, v) = \left(\frac{m_h}{2\pi}\right)^{3/2} \frac{n_f(s)}{T_f^{3/2}} \exp\left[-\frac{m_h v^2}{2T_f}\right] \tag{1}$$

where the ICRH power deposition profile is

$$T_f = T_e(1 + 3\xi/2), \tag{2}$$

$$\xi = \frac{P_{RF}(s)\tau_s}{3n_f(s)T_e}, \tag{3}$$

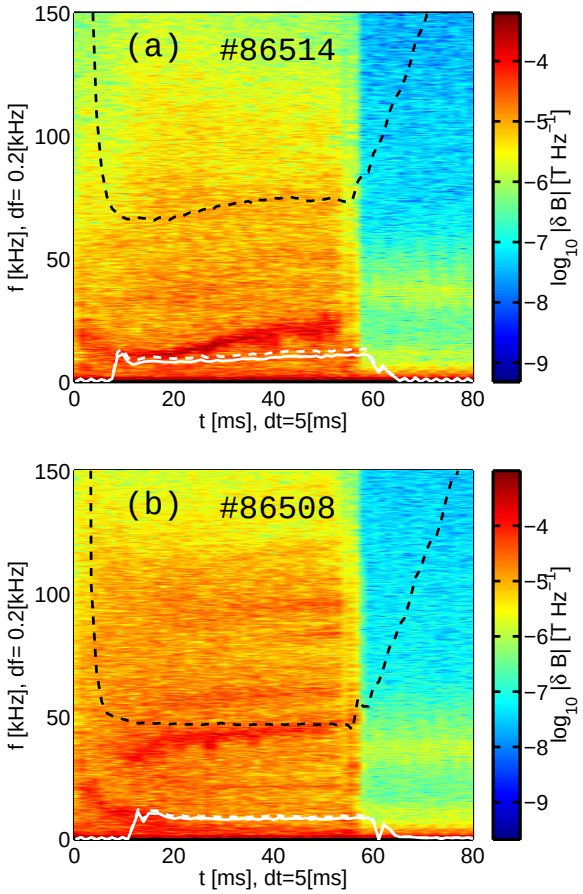

Figure 5. Spectrogram of magnetic fluctuations of (a) #86514 at 34kW RF power, and (b) #86508 at 80kW RF power. Also shown is the predicted evolution of a $(m, n) = (-4, 5)$ GAE mode (black dashed) and a $(m, n) = (-4, 5)$ BAE mode from scaling of the lowest BAE geodesic solution from Bertram *et al* [5] (white dashed) and ω_{CAP} (white solid).

$$\tau_s = \frac{3(2\pi)^{3/2}\epsilon_0^2 m_f T_e^{3/2}}{Z_h^2 e^4 m_e^{1/2} n_e \ln\Lambda} \tag{4}$$

with m_f the fast ion mass, n_f the fast ion density, T_f the fast ion temperature, Z_f the fast ion charge, $\ln\Lambda$ the Coulomb logarithm and e, ϵ_0 the electron charge and permittivity of free space, respectively. The time constant τ_s is the slowing down time and P_{RF} the RF power deposition profile, which we have chosen as $P_{RF}(s) = P_0 n_f(s)/n_{f0}$ with $P_0 = P_{tot}/V$, where V is the total plasma volume, and n_{f0} the on-axis fast ion density. The assumptions underpinning this assumption are two-fold: all RF power is absorbed, and power is transferred to preferentially heat the fast ions. With these substitutions, Eq. (3) becomes

$$\xi = \frac{P_{tot}\tau_s}{3V n_{f0} T_e}.$$

The thermalised ions are assumed to have the same temperature as the electrons, so $T_i = T_e$. We recognise that this is a simple heating model which does not capture the

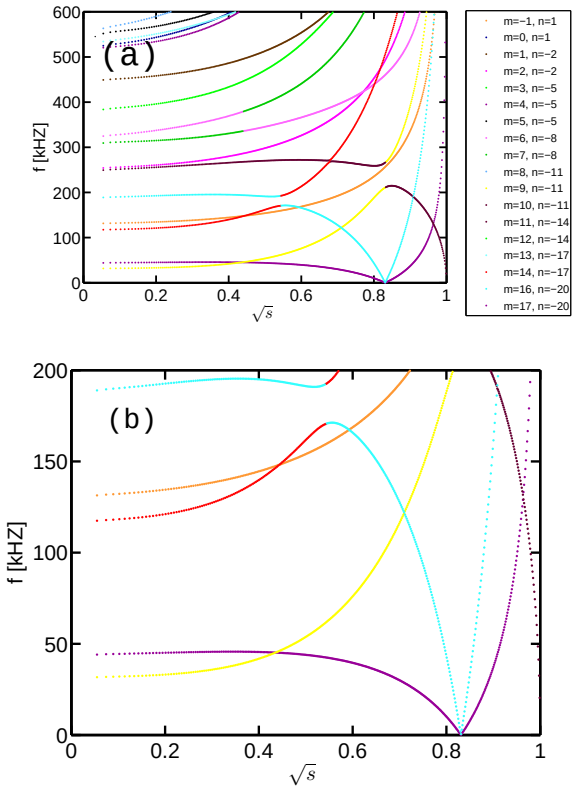

Figure 6. The shear Alfvén continuum with γ, the ratio of specific heats set to $\gamma = 0$ for $\kappa_H = 0.33$, as a function of the square root of normalised toroidal flux, $\sqrt{s}$. Figure (b) is a zoomed version of Figure (a) around the experimentally observed frequency range. The legend is common to both Figures.

full complexity of minority resonant fast ion heating in stellarator geometry. It is a scoping model used to establish trends.

For ICRH heated H-1 plasmas $V \approx 1$ m^3 and we take $T_e = 10$ eV, consistent with observations in Fig. 4. We have used Eqs. (2) to (4) to compute T_f. Figure 7 shows the computed electron density and perpendicular temperature as a function of RF power, and for different fast particle fractions n_f/n_e both for the experimental data and a parametrisation where $n_{e0} \propto P_{tot}$. The inverse dependency of T_f with P_{tot} can be seen from Eq. (3) and (4). In the linear case where $n_{e0} \propto P_{tot}$, the inverse dependence is governed by the inverse dependence of τ_s with n_e. As the density lowers, the slowing down time increases, producing a hotter minority tail. The tail becomes cooler as the fast particle population n_f/n_e increases. Experimentally, there is a change in slope in n_e versus P_{tot} at 50kW: above this threshold the electron density rises more slowly with RF power. This explains the plateau in T_f above 50kW. Additionally, the confinement of such fast ions must be considered in the complicated magnetic topology of H-1 : ρ/a the ratio of the gyroradius to the plasma minor radius is still only 0.13 at $T_f = 2$keV. However, energetic, non-collisional deeply trapped orbits characteristic of perpendicularly heated fast ions might depart the plasma within a couple of bounces.

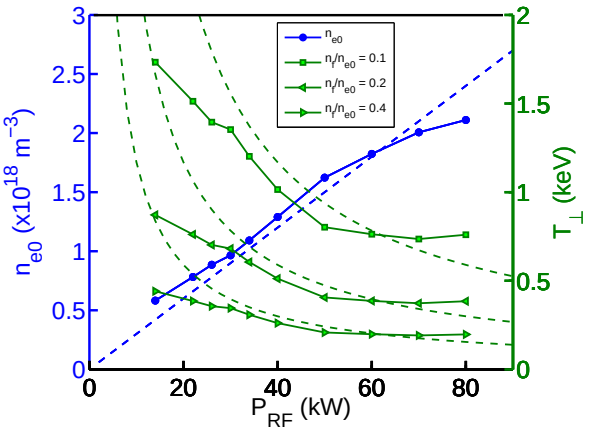

Figure 7. Electron density and computed perpendicular temperature as a function of RF power, and for different fast ion density n_f (solid). Also shown are temperature contours for the parametrisation $n_{e0} = 0.03 P_{tot} \times 10^{18}\mathrm{m}^{-3}$, with P_{tot} in kWatts (dashed).

3.1. Flux surface stability

Kolesnichenko *et al* [38] have computed an expression for the drive of Alfvénic instabilities due to circulating particles in optimised stellarators. The drive for such instabilities comes from velocity and spatial gradients in the distribution function $f_0(s, v)$ for energetic ions. The code LGRO [31] follows a similar derivation to Kolesnichenko *et al* . For the case of waves strongly localised to a flux surface and an isotropic distribution of energetic ions, the following growth rate is obtained (cf Eq. (40) of [38]):

$$\frac{\gamma}{\omega} = \frac{3\pi\beta_f R^2}{64(m\iota^* + n)^2 r^{*2}} \sum_{m',n',j=\pm 1} \frac{B_{m'n'}}{B_{0,0}} \frac{w \int_w^\infty duu(u^2+w^2)^2(\omega\frac{\partial f_0}{\partial u^2} + \omega_d f_0)}{\int_0^\infty duu^4 f_0} \quad (5)$$

with $u = v/v_0$, ω_d the fast ion diamagnetic drift frequency

$$\omega_d = \frac{m}{r}\frac{T_f}{eZ_f B}\frac{\partial \ln n_f}{\partial r} \quad (6)$$

and the term $w = v_{||}^{res}/v_0$ given by

$$w = \frac{1}{(1 + j\frac{m'\iota^* + n'N_p}{m\iota^* + n})\frac{v_0}{v_A}} \quad (7)$$

which encodes the resonance condition

$$v_{||}^{res} = v_A \left| 1 \pm \frac{m'\iota^* + n'N_p}{m\iota^* + n} \right|^{-1} \quad (8)$$

Here, β_f is the fast ion species β, $v_0 = \sqrt{2T_f/M_f}$ is the characteristic speed of the energetic ions, N_p the number of field periods of the machine, ι^* labels the local value of the rotational transform where the Alfvén branches cross, r^* the radial position of

the crossing, and m', n' label the component $B_{m'n'}(s)$, which are the Fourier harmonics of the magnetic field

$$\frac{B}{B_{00}} = 1 + \sum_{m',n'} \frac{B_{m'n'}(s)}{B_{00}} \cos(m'\vartheta - n' N_p \varphi) \tag{9}$$

in flux coordinates (r, ϑ, φ) seen by the particle. In Eq. (9) B_{00} is the average magnetic field at the magnetic axis.

As the fast ion distribution function is an isotropic Maxwellian in velocity, drive is due solely to the spatial gradient in the fast ion density: this appears as a non-zero ω_d in Eq. (5). As will be assumed later, the fast ion density is not homogenous, and takes the same functional form as the thermal ion density.

The code LGRO computes the cylindrical continuum

$$\omega_{m,n}^2 = k_{||}(m,n)^2 v_A^2 = \frac{(m\iota^* + n)^2}{R_0^2} v_A^2, \tag{10}$$

and identifies crossings between the (m, n) and $(m + \Delta m, n + \Delta n)$ branches. Crossings of different branches lie at $\omega_{m,n}^2 = \omega_{m+\Delta m, n+\Delta n}^2$ such that

$$(m\iota^* + n)^2 = ((m + \Delta m)\iota^* + (n + \Delta n))^2 \tag{11}$$

Solving yields

$$\iota^* = \begin{cases} -\left(\frac{2n+\Delta n}{2m+\Delta m}\right) & \Delta m \neq 0, \Delta n \neq 0 \\ \iota(s_m) & \Delta m = \Delta n = 0 \end{cases} \tag{12}$$

with s_m such that the frequency is chosen to be the minimum or maximum of the $\omega_{m,n}$ continuum frequency. The GAE gap is given by $(\Delta m, \Delta n) = (0, 0)$. The continuum branch is given by Eq. (10), which for H-1 ι profile yields a maximum in frequency near the core. Particles with speeds $v_{||}^{res}$ given by the resonance condition can hence drive the mode. That is,

$$\frac{v_{||}^{res}}{v_A} = \left| \frac{m\iota^* + n}{(m \pm m')\iota^* + (n \pm n' N_p)} \right| \tag{13}$$

The dominant contributions of $B_{m',n'}$ are determined by computing the Fourier expansion of $B_{m,n}$ for $m = 4, n = -5$ and $\kappa_H = 0.33$, as shown in Fig. 8. By inspection, the largest contributions are the $(m', n') = (1, 0), (1, -1)$ and $(1, -2)$ components. The GAE resides at the stationary point in the Alfvén frequency, located at a radial localisation of $s = 0.116$. At this location $\iota^* = 1.2289$. Table 1 computes $v_{||}^{res}/v_A$ for these (m', n') Fourier terms, together with the corresponding resonant energy $E^{res} = m_H (v_{||}^{res})^2/2$ and the fast ion growth rate contribution γ_{fast}.

We have used LGRO [31] to compute the growth linear growth / damping rate for the electron, ion and fast ion species, as well as the total growth rate. The composition of H-1 plasmas for the scans conducted in this work is a hydrogen and helium mixture with a H:2He gas flow ratio. We have modelled the ion species as a single fluid with mass $\approx 3m_H$, (allowing for a small amount of oxygen and carbon impurity) and a hydrogen fast particle population. The ion temperature $T_i = 10$ eV profile is assumed constant,

$v_{\|\|}^{res}/v_A$	E^{res} (eV)	(m', n')	sign	γ_{fast} (s^{-1})
0.0737	512	(1,0)	+	2.02×10^3
0.0643	389	(1,0)	-	1.63×10^3
0.0455	195	(1,-1)	+	642
0.0500	236	(1,-1)	-	736
0.0174	28	(1,-2)	+	194
0.0180	31	(1,-2)	-	207

Table 1. Table of circulating particle speed and corresponding energy $E^{res} = m_H(v_{||}^{res})^2/2$ to satisfy the resonance condition for the (m', n') component and sign. Also given is the contribution γ_{fast}. The calculation of resonant energy uses hydrogen mass for the minority species. The calculation of v_A assumes $m_{H1} \approx 3m_H$, which is the effective mass of the single fluid plasma.

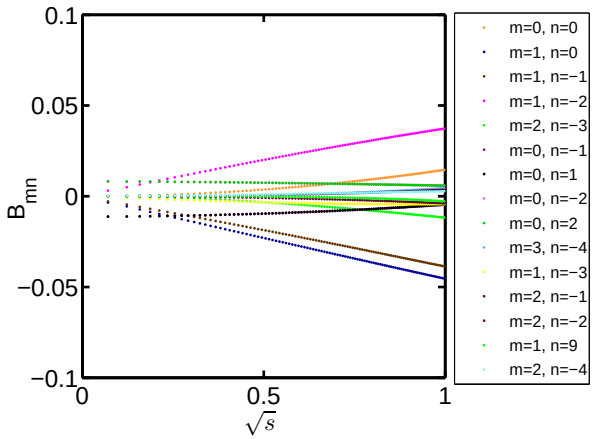

Figure 8. Fourier components of the magnetic field strength in Boozer coordinates for H-1 and $\kappa_H = 0.33$, as a function of square root of normalised toroidal flux $\sqrt{s}$.

and the ion density and fast ion density assume a $(1 - s)$ dependence. Due to the comparatively low electron temperature, the population of He++ is very small, and so the charge state of all ion species is 1.

A Maxwellian distribution function is assumed for the electrons, ions and fast ions. Finally, the three largest (m', n') components identified in Fig. 8 are provided, and the growth rate summed over these components. The fast ion growth rate matches the sum of γ_{fast} in Table 1. We have confirmed that the inclusion of the next three largest harmonics changes the growth rate by less than 1.4%. Figure 9 shows the linear growth / damping rate for the electron, ion and fast ion species, as well as the total growth rate for the 80 kW case with $n_f/n_0 = 0.1$ and $n_0 = 2.2 \times 10^{18}$ m^{-3} for the three lowest frequency modes. The mode with the largest growth rate is $(m, n) = (4, -5)$ with $(\Delta m, \Delta n) = (0, 0)$: this is a GAE. For this mode the fast ion drive is dominant, with weak ion and electron damping: $-\gamma_i/\gamma_{fast} < 1\%$ and $-\gamma_e/\gamma_{fast} < 0.5\%$.

We have also investigated the dependence of linear drive $\gamma_{tot} = \gamma_i + \gamma_e + \gamma_{fast}$ on fast ion temperature, density, and RF power relative to the case studied in Fig. 9. Figure

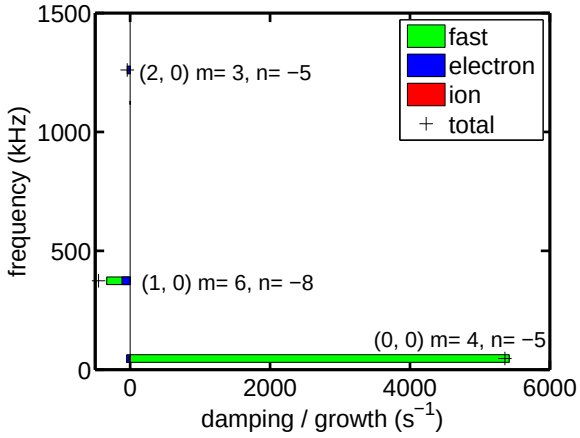

Figure 9. Damping / growth for the electron, ion and fast ion species, as well as the total growth rate as a function of frequency. The prefix of each mode is labelled $(\Delta m, \Delta n)$, thereby identifying the gap in which the mode is located. The GAE gap is $(\Delta m, \Delta n) = (0, 0)$, the toroidicity induced gap is $(\Delta m, \Delta n) = (1, 0)$, and the ellipticity induced gap is $(\Delta m, \Delta n) = (2, 0)$.

10 shows the variation in growth rate with fast ion temperature for $n_f/n_0 = 0.1$. The growth rate is proportional to β_{fast}, and the mode is unstable for $T_f > 350$ eV. The mode frequency is independent of β_{fast}, and so the frequency is unchanged at 47 kHz across the scan.

Figure 11 shows the variation in growth rate and fast particle temperature as n_f/n_0 is varied. For $n_f/n_0 < 0.20$ the mode is driven unstable. In H-1 the RF power both heats the plasma and is responsible for its formation, and so n_f/n_0 is not an independent parameter. The total density is not varied across the scan, so the mode frequency remains at 47 kHz.

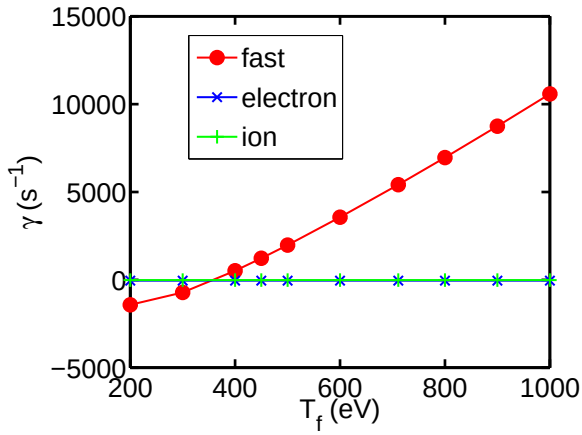

Figure 10. Parameter scan of the local linear growth rate as a function of T_f obtained using LGRO. Other conditions (power, density) are the same as in Fig. 9

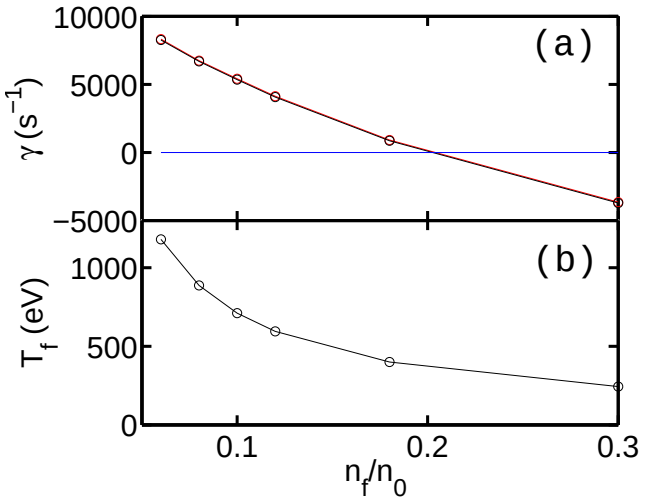

Figure 11. Parameter scan of (a) linear growth rate and (b) fast ion temperature with n_f/n_0. Other conditions are the same as in Fig. 9

3.2. Global stability

We consider the stability of a GAE in the H-1 stellarator under the influence of fast particles numerically. The mode structure is computed by the ideal MHD eigenvalue code CKA, and subsequently used in EUTERPE, a gyrokinetic code to compute the growth rate.

For a given VMEC solution, CKA can solve for the mode in either Boozer or PEST magnetic coordinates, while at the present time EUTERPE requires PEST coordinates. H-1 equilibria are particularly numerically challenging, with large uncertainties in the VMEC equilibrium quantities computed near the axis. For the construction of Boozer coordinates, we use a reliable mapping by Nührenberg, [39] together with the Improve code. The latter takes fluxes and three of the metric components extrapolates them as theory predicts towards the axis and then recalculates the full metric consistently. For the PEST coordinate system we use the mapping for EUTERPE which was developed in parallel with EUTERPE. This mapping uses a smoothing of R and Z calculated by VMEC as proposed by the Graz group [40]. In both cases the uncertainties in the VMEC equilibrium quantities computed near the axis also caused a spurious continuum resonance in numerical eigenmode solutions. We eliminate this feature by adjusting the density profile near the core from the $(1-s)$ dependence used so far. In this section and next a density profile of $(1+\Delta_1 \exp(-\Delta_2\sqrt{s}))(1-s)$ is adopted, with $\Delta_1 = 0.2$ and $\Delta_2 = 43.8$.

Figure 12 shows the perturbed electrostatic potential obtained by CKA in both Boozer and PEST coordinates. The frequency of this mode is 40.9 kHz (Boozer) and 38 kHZ (PEST). The Fourier spectrum of the two modes are near identical, the frequencies very close, and the peak of the $(m,n) = (-4,5)$ mode at the same radial location. The most significant difference is that mode computed using PEST coordinates

is slightly narrower. We attribute the differences between the modes to be a mixture of the not well converged equilibrium near the axis with the different smoothing applied to Boozer and PEST coordinates.

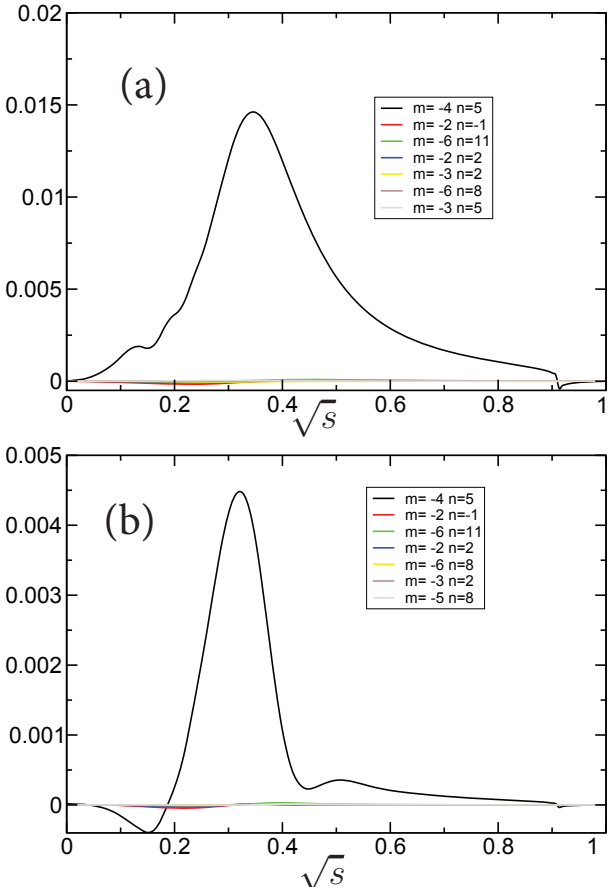

Figure 12. The perturbed electrostatic potential obtained by CKA as a function of $\sqrt{s}$ in (a) Boozer and (b) PEST coordinates

EUTERPE is a gyrokinetic code which can be used to model the wave-particle interaction of a population of energetic particles with fixed, prescribed fields. The mode structure in Fig. 12(b) has been passed to EUTERPE as a prescribed field perturbation, along with the same H-1 equilibrium as in the CKA calculation. Its interaction with a Maxwellian population of energetic particles with density $n_f/n_0 = 0.1$ and temperature T_f varying in the range $10 < T_f < 5000$ eV has been simulated. These simulations have been repeated both with physical Larmor radius and with vanishing Larmor radius.

The growth rate is found to vary with fast particle temperature, as shown in Figure 13. A peak is seen in the growth rate around $T_f = 1700$ eV with both physical and zero Larmor radius. The marginal stability point calculated with zero Larmor radius agrees well with LGRO, which is to be expected as the marginal point is determined by the condition $\omega \approx \omega_*$. Consistent with observations in W7-X and W7-AS the calculated LGRO growth rates are larger than those of the global calculation, since the global calculation also averages over radial positions where the mode amplitude is smaller.

The inclusion of finite Larmor radius effects increases the marginal stability point by a factor of two, and reduces the growth rate where the mode is unstable by up to a factor of 10. For these plasma conditions the Larmor radius of the thermal ions is 0.1 cm, and for the fast ions at marginal stability point of 750 eV it is 1 cm. The latter is 5% of the minor radius in the vertical direction, and so finite Larmor radius effects are indeed likely to be significant. Finally, the roll-over in growth rate at $T_f \approx 1700$ eV happens when the fast particle orbit widths become comparable to the mode width. [41]

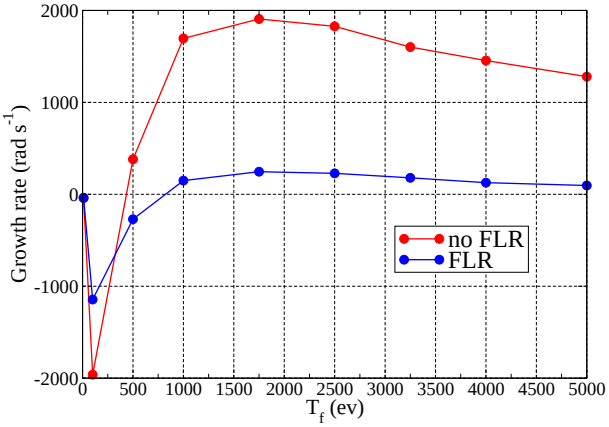

Figure 13. Linear growth rate as a function of fast particle temperature for the $(m, n) = (4, -5)$ mode computed with EUTERPE.

3.3. Damping

Finally, we calculate the damping of the global mode due to interaction with the thermal plasma. In the ideal MHD limit, damping occurs due to the continuum resonance at the edge of the plasma. Inclusion of finite Larmor radius and parallel electric field effects introduces additional damping. These calculations are the first time continuum and resistive damping have been calculated based on stellarator experimental data.

We use a complex integration contour technique to compute continuum damping. This procedure involves analytic continuation of spatial variables in the complex domain [34]. Convergence must be shown with respect to contour deformation and spatial resolution. H-1 equilibria are particularly numerically challenging, with large errors in the equilibrium quantities computed near the core. These result in a sharp change in continuum resonance frequency, causing a spurious continuum resonance in numerical eigenmode solutions. We eliminate this feature by adjusting the density profile near the core from the $(1 - s)$ dependence used so far. In this section a density profile of $(1 + \Delta_1 \exp(-\Delta_2\sqrt{s}))(1 - s)$ is adopted, with $\Delta_1 = 0.2$ and $\Delta_2 = 43.8$. The resulting change in mode structure is plotted in figure 14.

Using a reduced ideal MHD expression for a periodic cylindrical plasma with negligible β, we have been able to find a set of separate $(4, -5)$ GAEs for the H-1 ι and ρ profiles.[37] These modes display anti-Sturmian behaviour and have an accumulation

point at the maximum of the continuum. The highest frequency mode is a broad GAE with zero radial nodes localised nearest to the plasma edge. The reduced ideal MHD wave equation of CKA is solved over a complex integration path in s, which is defined by

$$s = \left(t + i\alpha \exp\left(- \left(\frac{t - t_\beta}{t_\gamma} \right)^2 \right) \right)^2 . \tag{14}$$

Here the contour parameter is $t \in [0, 1]$. We let parameters $t_\beta = 0.92$ and $t_\gamma = 0.1$, defining the location and width of the deformation from the real s axis. The parameter α is varied to test convergence with respect to contour deformation. Plasma pressure gradient and compressibility are neglected, based on the very low β in this case ($\sim 10^{-4}$). The parallel component of the equilibrium current is also neglected, as it is assumed to be small in the absence of external current drive. Inclusion of the parallel current term in the wave equation is found to cause numerical convergence problems, presumably because it is poorly modelled near the core resulting in spurious couplings to additional Fourier harmonics.

Applying this method, a mode with complex frequency $40.3 - 0.0418i$ kHz is obtained, corresponding to a normalised continuum damping of $\gamma/\omega = 1.04 \times 10^{-3}$. This value can be shown to be well converged for radial, poloidal and toroidal resolutions of $N_s = 80$, $N_\theta = 40$ and $N_\phi = 20$ respectively and $\alpha = 1.0$. When resolution is changed to $N_s = 120$, $N_\theta = 30$ or $N_\phi = 15$ γ/ω changes by 0.106%, 0.136% and -0.0730% of its value respectively. Variation in α between 0.2 and 1.0 results in γ/ω varying by less than 0.193%. Changing the density profile such that $\Delta_1 = 0.3$ results in a difference in γ/ω of 1.58%, demonstrating that damping is not significantly affected by the artificial change in density profile.

Applying a similar method to the cylindrical incompressible plasma model results in estimated complex frequency $55.1 - 0.0173i$ kHz, and thus continuum damping of $\gamma/\omega = 3.15 \times 10^{-4}$. It is evident that three-dimensional geometry significantly affects both frequency and damping of the mode.

Finite Larmor radius and parallel electric field effects can be included in CKA through kinetic extensions to the polarisation operator.[42] This includes a dissipative term, which can be calculated based on the kinetic model described by Fu *et al.*.[43] In an H-1 plasma with $T_e = 10eV$ and $n_i = n_e = 2.2 \times 10^{18}$ m^{-3}, assuming a Maxwellian velocity distribution, the electron-ion collision frequency $\nu_{ei} = 2.5$ MHz, which is much larger than the mode frequency. Moreover, the electron mean free path of approximately 0.75 m is much shorter than $k_\parallel^{-1} = 13$ m. Consequently, the kinetic model indicates that dissipation is primarily due to electron-ion collisionality with a smaller contribution from electron Landau damping. There is an effective resistivity of

$$\eta \approx \mu_0 \omega \rho_i^2 \frac{T_e}{T_i} \left(\frac{\omega}{k_\parallel v_A} \right)^2 \delta(\omega) , \tag{15}$$

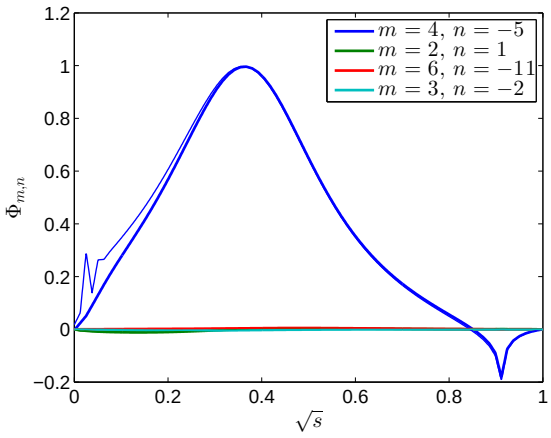

Figure 14. Mode eigenfunction using ideal MHD model for modified (thick line) and linear (thin line) density profiles, as a function of $\sqrt{s}$.

where

$$\delta(\omega) = \Im\left(\frac{1 + i\hat{\nu}Z(\xi)}{1 + \xi Z(\xi)}\right). \tag{16}$$

Here $Z(\xi)$ is the plasma dispersion function, $\xi = \frac{\omega + i\nu}{k_\parallel v_e}$ and $\hat{\nu} = \frac{\nu}{k_\parallel v_e}$. The function $\delta(\omega)$ is taken to be constant throughout the plasma, with $k_\parallel$ evaluated at the central peak of the mode. The non-linear frequency dependence of this function necessitates an iterative solution of the eigenvalue problem.

Resistivity is found to have converged within 0.22% after three iterations of CKA. Inclusion of resistive effects results in the calculation of a much larger damping, with complex frequency $38.1 - 7.19i$ kHz and $\gamma/\omega = -0.189$. This large damping is consistent with experimental observations that in absence of drive the mode decays rapidly on timescales ($\sim$ 0.1 ms). The mode, which is plotted in figure 15, is also broadened significantly by resistive effects. The real frequency component of the mode decreases and its maximum moves towards the edge of the plasma, better matching the $(4, -5)$ global mode observed in H-1. [22]

4. Conclusions

We have identified a transition in mode activity in H-1 mixed helium/hydrogen plasmas with increasing RF power. The mode activity transitions from BAE activity to GAE mode activity at around 50kW of ICRH heating. We have computed the mode continuum and identified nonconventional GAE structures using the ideal MHD solver CKA and gyrokinetic code EUTERPE. An analytic model for ICRH heated minority ions is used to estimate the fast ion temperature of the hydrogen species. A linear growth rate scan of local flux surface stability LGRO was performed in Fig. (10). These results reveal drive is possible with a small ($n_f/n_0 < 0.2$) hot energetic tail of the hydrogen species, for which $T_f > 300$ eV. These studies demonstrate drive from the radial spatial

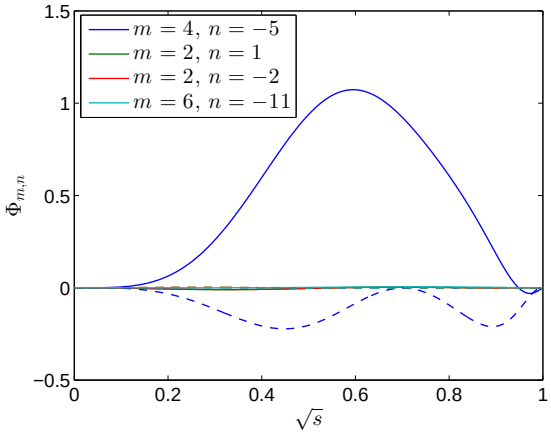

Figure 15. Mode eigenfunction using resistive MHD model including kinetic effects as a function of $\sqrt{s}$. The dashed and solid lines represent imaginary and real components.

gradient of circulating particles whose speed is significantly less than the Alfvén speed, and are resonant with the mode through harmonics of the Fourier decomposition of the field. Linear growth rate scans are also complemented with global kinetic calculations from EUTERPE in Fig. (13). These qualitatively confirm the findings from the LGRO study, and show a similar marginal stability point in the zero Larmor radius limit. Consistent with observations in W7-X and W7-AS the calculated LGRO growth rates are larger than those of the global calculation, since the global calculation also averages over radial positions where the mode amplitude is smaller. The inclusion of finite Larmor radius effects increases the marginal stability fast ion temperature by a factor of two, and reduces the growth rate where the mode is unstable by up to a factor of 10. Finally, the roll-over in growth rate at $T_f \approx 1700$ eV happens when the fast particle orbit widths become comparable to the mode width. [41]

A study of damping of the global mode with the thermal plasma is also conducted, computing continuum, and the damping arising from finite Larmor radius and parallel electric fields (via resistivity). We find that continuum damping is of order 0.1% for the configuration studied. A similar calculation in the cylindrical plasma model produces a frequency 35% higher and a damping 30% of the three dimensional result: this confirms the importance of strong magnetic shaping to the frequency and damping. Finally, the inclusion of resistivity lifts the damping to $\gamma/\omega = -0.189$. Such large damping is consistent with experimental observations that in absence of drive the mode decays rapidly (~ 0.1 ms). Indeed, we have modulated the RF heating power within the pulse and demonstrated that the GAE decays on the timescale of ≤ 0.1 ms, thereby validating theory predictions.

The analysis prompts several areas of future study. Analysis of the mode numbers of the suspected GAE is indeterminate. Mode tomography techniques pioneered by Haskey *et al* , or Langmuir probe scans would reveal insight into the mode numbers

and radial structure at higher power. The analysis performed here is for a particular choice of density profile, which, without Abel inversion, only approximately represents the spatial profile of the experimental density profile. Our calculations suggest that it is plausible the mode is unstable with a $1 - s$ density profile, since we calculate an unstable mode with at least some set of reasonable parameters. In general however, both drive and damping is a strong function of density profile. A study of drive and damping for a range of density profiles, as well as that obtained for the experimental profile obtained by full Abel inversion of the measured data, would not only validate the physics, but might suggest mode existence could also be used as a form of MHD spectroscopy. Measurements of the distribution function do not exist. This could be measured by a range of particle diagnostics (e.g. in situ Faraday cup, scintillator or neutral particle analyser). Varying the plasma gas mixture would confirm whether the simple mass dependence and hydrogen minority heating model of this analysis is correct.

Further work is also required to address the accuracy of VMEC near the magnetic axis and limitations of the use of PEST coordinates in EUTERPE. Work is in progress to transform the Boozer output of CKA directly to PEST coordinates to pipe it into EUTERPE.

Acknowledgments

This work was part funded by the Australian Government through Australian Research Council grant DP1401000790. This work has been carried out within the framework of the EUROfusion Consortium and has received funding from the Euratom research and training programme 2014-2018 under grant agreement No 633053. The views and opinions expressed herein do not necessarily reflect those of the European Commission. We received funding from the German Academic Exchange service under contract numbers 50753864 and 57060539.

References

[1] H. H. Duong, W. W. Heidbrink, E. J. Strait, T. W. Petrie, R. Lee, R. A. Moyer, and J. G. Watkins. Loss of energetic beam ions during TAE instabilities. *Nucl. Fusion*, pages 749–765, 1993.

[2] M. J. Hole and M. Fitzgerald. Resolving the wave-particle-plasma interaction: advances in the diagnosis, interpretation and self-consistent modelling of waves, particles and the plasma configuration. *Plasma Phys. Control. Fusion*, 2014.

[3] S. D. Pinches, H. L. Berk, D. N. Borba, B. N. Breizman, S. Briguglio, A. Fasoli, G. Fogaccia, M. P. Gryaznevich, V. Kiptily, M. J. Mantsinen, S. E. Sharapov, D. Testa, R. G. L. Vann, G. Vlad, F. Zonca, and JET-EFDA Contributors. The role of energetic particles in fusion plasmas. *Plasma Phys. Control. Fusion*, 2004.

[4] M. J. Hole, C. M. Ryu, M. H. Woo, J. G. Bak, S. E. Sharapov, M. Fitzgerald, and the KSTAR Team. First evidence of Alfvén wave activity in KSTAR plasmas. *Plasma Phys. Control. Fusion*, 55:045004, 2013.

[5] J. Bertram, B. D. Blackwell, and M. J. Hole. Ideal-magnetohydrodynamic theory of low-frequency Alfvén waves in the H-1 Heliac. *Plasma Phys. Control. Fusion*, 54:055009, 2012.

[6] A. Weller, D. A. Spong, R. Jaenicke, A. Lazaros, F. P. Penningsfeld, S. Sattler, W7-AS Team, and NBI Group. Neutral Beam Driven Global Alfvén Eigenmodes in the Wendelstein W7-AS Stellarator. *Phys. Rev. Lett.*, 72(8):1220–1223, 1994.

[7] S. Yamamoto, K. Toi, N. Nakajima, S. Ohdachi, S. Sakakibara, K. Y. Watanabe, M. Goto, K. I keda, O. Kaneko, K. Kawahata, S. Masuzaki, T. Morisaki, S. Morita, S. Murakami, K. Narihara, Y. Oka, M. Osakabe, Y. Takeiri, K. Tanaka, T. Tokuzawa, K. Tsumori, H. Yamada, I. Yamada, K. Yamazaki, and LHD Experimental Group. Observation of Helicity-Induced Alfvén Eigenmodes in Large-Helical-Device Plasmas Heated by Neutral-Beam Injection. *Phys. Rev. Lett.*, 91(24):245001, 2003.

[8] S. Yamamoto, K. Toi, S. Ohdachi, N. Nakajima, S. Sakakibara, C. Nührenberg, K.Y. Watanabe, S. Murakami, M. Osakabe, M. Goto, K. Kawahata, S. Masuzaki, S. Morita, K. Narihara, Y. Narushima, N. Ohyabu, Y. Takeiri, K. Tanaka, T. Tokuzawa, H. Yamada, I. Yamada, K. Yamazaki, and LHD experimental group. Experimental studies of energetic-ion-driven MHD instabilities in Large Helical Device plasmas. *Nucl. Fusion*, 45:326–336, 2005.

[9] K Toi, S Yamamoto, N Nakajima, S Ohdachi, S Sakakibara, M Osakabe, S Murakami, K Y Watanabe, M Goto, K Kawahata, Ya I Kolesnichenko, S Masuzaki, S Morita, K Narihara, Y Narushima, Y Takeiri, K Tanaka, T Tokuzawa, H Yamada, I Yamada, K Yamazaki, and LHD Experimental Group. Energetic ion driven Alfvén eigenmodes in Large Helical Device plasmas with three-dimensional magnetic structure and their impact on energetic ion transport. *Plasma Phys. Control. Fusion*, 46:S1–S13, 2004.

[10] R. Jiméenez-Gómez, A. Könies, E. Ascasíbar, F. Castejón, T. Estrada, L. G. Eliseev, A. V. Melnikov, J.A. Jiménez, D. G. Pretty, D.Jiménez-Rey, M.A. Pedrosa, A. de Bustos, and S. Yamamoto. Alfvén eigenmodes measured in the TJ-II stellarator. *Nucl. Fusion*, 51:033001, 2011.

[11] W. W. Heidbrink, E. Ruskov, E. M. Carolipio, J. Fang, and M. A. van Zeeland. What is the beta-induced Alfvén eigenmode? *Phys. Plas.*, 6(4):1147–1161, 1999.

[12] S. Hamberger, B. D. Blackwell, L. Sharp, and D. Shenton. H-1 Design and Construction. *Fusion Technology*, 17:123, 1990.

[13] J. H. Harris, M. G. Shats, B. D. Blackwell, W. M. Solomon, D. G. Petty, S. M. Collis, J. Howard, H. Xia, C. A. Michael, and H. Punxmann. Fluctuations and stability of plasmas in the H-1NF heliac. *Nucl. Fus.*, 44:279–286, 2004.

[14] D. G. Pretty. *A study of MHD activity in the H-1 heliac using data mining techniques*. PhD thesis, Research School of Physics and Engineering, Australian National University, 2007.

[15] B.D. Blackwell, D.G. Pretty, J. Howard, R. Nazikian, S.T.A. Kumar, D. Oliver, D. Byrne, J.H. Harris, C.A. Nuhrenberg, M. McGann, R.L. Dewar, F. Detering, M. Hegland, G.I. Potter, and J.W. Read. Configurational Effects on Alfvénic modes and Confinement in the H-1NF Heliac. https://arxiv.org/abs/0902.4728, 2009.

[16] D. G. Pretty and B. D. Blackwell. A data mining algorithm for automated characterisation of fluctuations in multichannel timeseries. *Computer Physics Communications*, 180:1768–1776, 2009.

[17] S. R. Haskey, B. D. Blackwell, B. Seiwald, M. J. Hole, D. G. Pretty, J. Howard, and J. Wach. A multichannel magnetic probe system for analysing magnetic fluctuations in helical axis plasmas. *Rev. Sci. Instrum.*, 84:093501, 2013.

[18] S. R. Haskey, N. Thapar, B. D. Blackwell, and J. Howard. Synchronous imaging of coherent plasma fluctuations. *Rev. Sci. Instrum*, 85:033505, 2014.

[19] S.R.Haskey, B.D.Blackwell, and D.G.Pretty. Clustering of periodic multichannel time series data with application to plasma fluctuations. *Computer Physics Communications*, 185:1669–1680, 2014.

[20] S.R. Haskey, B.D. Blackwell, B. Seiwald, and J. Howard. Visible light tomography of MHD eigenmodes in the H-1NF stellarator using magnetic coordinates. *Nucl. Fusion*, 54:083031, 2014.

[21] J. Bertram, M. J. Hole, D. G. Pretty, B. D. Blackwell, and R. L. Dewar. A reduced global Alfvén eigenmodes model for Mirnov array data on the H-1NF heliac. *Plasma Phys. Control. Fusion*, 53:085023, 2011.

[22] S. R. Haskey, B. D. Blackwell, C. Nührenberg, A. Könies, J. Bertram, C. Michael, M. J. Hole, and J. Howard. Experiment-theory comparison for low frequency BAE modes in the strongly shaped H-1NF stellarator. *Plasma Phys. Control. Fusion*, 57:095011, 2015.

[23] C. Schwab. Ideal magnetohydrodynamics: global mode analysis of three-dimensional plasma configurations. *Phys. Fluids B*, 1993.

[24] A. Könies and D. Eremin. Coupling of Alfvén and sound waves in stellarator plasmas. *Phys. Plas.*, 17:012107, 2010.

[25] S. Ma, J. Howard, B. D. Blackwell, and N. Thapa. Measurements of electron density and temperature in the H-1 heliac plasma by helium line intensity ratios. *Rev. Sci. Instrum.*, 83:033102, 2012.

[26] A.V. Melnikov, L.G. Eliseev, R. Jiménez-Gómez, E. Ascasibar, C. Hidalgo, A.A. Chmyga, A.D. Komarov, A.S. Kozachok, I.A. Krasilnikov, S.M. Khrebtov, L.I. Krupnik, M. Liniers, S.E. Lysenko, V.A. Mavrin, J.L. de Pablos, M.A. Pedrosa, S.V. Perfilov, M.V. Ufimtsev, T. Ido, K. Nagaoka, S. Yamamoto, Yu.I. Taschev, A.I. Zhezhera, and A.I. Smolyakov. Internal measurements of Alfvén eigenmodes with heavy ion beam probing in toroidal plasmas. *Nuc. Fus.*, 2010.

[27] Ya. I. Kolesnichenko and V. V. Lutsenko. Conventional and nonconventional global Alfvï¿½n eigenmodes in stellarators. *Physics of Plasmas*, 14:102504, 2007.

[28] A. Mishchenko, A. Könies, T. Feher, R. Kleiber, M. Borchardt, J. Riemann, R. Hatzky, J. Geiger, and Yu. Turkin. Global hybrid-gyrokinetic simulations of fast-particle effects on Alfvén Eigenmodes in stellarators. *Nuc. Fus.*, 54:104003, 2014.

[29] R. O. Dendy, R. J. Hastie, K. G. McClements, and T. J. Martin. A model for ideal m=1 internal kink stabilization by minority ion cyclotron resonant heating. *Phys. Plasmas*, 2:1623, 1995.

[30] T.H. Stix. Fast-wave heating of a two-component plasma. *Nucl. Fus.*, 15:737–754, 1975.

[31] A. Könies, A. Mishchenko, and R. Hatzky. From kinetic MHD in stellarators to a fully kinetic description of wave particle interaction. In *Theory of Fusion Plasmas, AIP Conference Proceedings*, volume 1069, page 133, 2008.

[32] Axel Könies. A code for the calculation of kinetic Alfvén waves in three-dimensional Geometry. In *10th IAEA TM on Energetic Particles in Magnetic Confinement Systems*, 2007.

[33] G. Jost, T. M. Tran, W. A. Cooper, L. Villard, and K. Appert. Global linear gyrokinetic simulations in quasi-symmetric configurations. *Phys. Plas.*, 8(7):3321–3333, 2001.

[34] G. W. Bowden, M. J. Hole, and A. Könies. Calculation of continuum damping of Alfvén eigenmodes in tokamak and stellarator equilibria. *Physics of Plasmas*, 22:092114, 2015.

[35] C. A. Michael, F. Zhao, B. D. Blackwell, M. F. J. Vos, J. Brotankova, S. R. Haskey, B. Seiwald, and J Howard. Influence of magnetic configuration on edge turbulence and transport in the H-1 Heliac. *Plasma Phys. Control. Fusion*, 2017.

[36] F. Zonca, L. Chen, and R. A. Santoro. Kinetic theory of low-frequency Alfvén modes in tokamaks. *Plas. Phys. Con. Fus.*, 38:2011–2028, 1996.

[37] Y. I. Kolesnichenko, V. V. Lutsenko, A. Weller, A. Werner, Y. V. Yakovenko, J. Geiger, and O. P. Fesenyuk. Conventional and nonconventional global Alfvén eigenmodes in stellarators. *Physics of Plasmas*, 14(10):102504, 2007.

[38] Ya. I. Kolesnichenko, V. V. Lutsenko, H. Wobig, and V. Yakovenko. Alfvén instabilities driven by circulating ions in optimized stellarators and their possible consequences in a Helias reactor. *Phys. Plas.*, 9:517, 2002.

[39] J. Nührenberg and R. Zille. In *Theory of Fusion Plasmas, Varenna*, page 3. Editrice Compositori, Bologna, 1988, 1987. EUR 11336 EN.

[40] Bernhard Seiwald, Georg Leitold, Winfried Kernbichler, and Sergei Kasilov. Consistent Recalculation of MHD Equilibria from VMEC. In *Annual symposium of the Austrian Physical*

Society, 2001.

[41] N. N. Gorelenkov, C. Z. Cheng, and G. Y. Fu. Fast particle finite orbit width and Larmor radius effects on low-n toroidicity induced Alfvén eigenmode excitation. *Physics of Plasmas*, 1999.

[42] T. Fehér. *Simulation of the interaction between Alfvén waves and fast particles.* PhD thesis, University of Greifswald, November 2013.

[43] G. Y. Fu, H. L. Berk, and A. Pletzer. Kinetic damping of toroidal Alfvén eigenmodes. *Physics of Plasmas (1994-present)*, 12(8):082505, 2005.